Icarus 228 (2014) 86–95

Contents lists available at ScienceDirect

Icarus

journal homepage: www.elsevier.com/locate/icarus

Enhanced sodium abundance in Mercury's north polar region revealed by the MESSENGER Gamma-Ray Spectrometer

Patrick N. Peplowski [a,*], Larry G. Evans [b], Karen R. Stockstill-Cahill [a,c], David J. Lawrence [a], John O. Goldsten [a], Timothy J. McCoy [c], Larry R. Nittler [d], Sean C. Solomon [d,e], Ann L. Sprague [f], Richard D. Starr [g], Shoshana Z. Weider [d]

[a] The Johns Hopkins University Applied Physics Laboratory, Laurel, MD 20723, USA
[b] Computer Science Corporation, Lanham-Seabrook, MD 20706, USA
[c] National Museum of Natural History, Smithsonian Institution, Washington, DC 20013, USA
[d] Department of Terrestrial Magnetism, Carnegie Institution of Washington, Washington, DC 20015, USA
[e] Lamont-Doherty Earth Observatory, Columbia University, Palisades, NY 10964, USA
[f] Lunar and Planetary Laboratory, University of Arizona, Tucson, AZ 85721, USA
[g] Physics Department, Catholic University of America, Washington, DC 20064, USA

ARTICLE INFO

Article history:
Received 3 July 2013
Revised 4 September 2013
Accepted 6 September 2013
Available online 21 September 2013

Keywords:
Mercury
Gamma-ray spectroscopy
Mercury, surface

ABSTRACT

MESSENGER Gamma-Ray Spectrometer measurements demonstrate that the abundance of Na varies across the surface of Mercury. The maximum Na/Si abundance ratio of 0.20 ± 0.03 by weight (~5 wt% Na) is observed at high northern latitudes and is significantly larger than the equatorial Na/Si ratio of 0.11 ± 0.01 (~2.6 wt% Na). Comparisons of forward-modeled surface distributions with the gamma-ray measurements suggest that the observed distribution of Na can be explained by differences in elemental composition between the volcanic smooth plains units and heavily cratered terrain. The comparison improves when thermally driven depletion of Na from areas near Mercury's hot poles is included. When combined with other MESSENGER data sets, these results indicate that the smooth plains units include substantial abundances of alkali feldspars. Thermal depletion of Na from the hot poles without an assumed underlying compositional variability can also reproduce the measured Na/Si distribution, but that mechanism fails to account for other MESSENGER observations that support the presence of higher abundances of feldspars in the smooth plains units.

1. Introduction

The nature and origin of moderately volatile lithophile elements on the surface of Mercury are long-standing questions. Their present-day crustal abundances were predicted to be near zero on the basis of formation mechanisms developed to explain Mercury's high metal-to-silicate ratio (e.g., Taylor and Scott, 2003). Under these formation hypotheses, high-temperature processes yielded a planet with a high bulk ratio of metal to silicate as well as a bulk composition depleted in moderately volatile elements. Decades of terrestrial and space-based observations of Mercury's exosphere, however, have revealed appreciable amounts of the moderately volatile species Na (Potter and Morgan, 1985) and K (Potter and Morgan, 1986). As the constituents of the exosphere are largely derived from surface material (Domingue et al., 2007, and references therein), these observations have been in apparent conflict with the expectation of a surface depleted in moderately volatile lithophile elements.

Prior to the insertion of the MErcury Surface, Space ENvironment, GEochemistry, and Ranging (MESSENGER) spacecraft in orbit about Mercury in March 2011, the composition of Mercury's surface was largely unconstrained and its volatile content was unknown. MESSENGER carries an extensive payload of scientific instruments designed, in part, to investigate the elemental composition of Mercury's surface (Solomon et al., 2007). Orbital measurements of the surface composition made by the X-Ray Spectrometer (XRS; Schlemm et al., 2007) and Gamma-Ray Spectrometer (GRS; Goldsten et al., 2007) have led to the discovery of higher-than-expected abundances of the moderately volatile elements S (Nittler et al., 2011; Weider et al., 2012; Evans et al., 2012) and Na (Evans et al., 2012) on Mercury's surface. Additionally, measurements of the K/Th ratio indicate that the surface is not depleted in moderately volatile elements relative to refractory elements when compared with the other terrestrial planets (Peplowski et al., 2011b, 2012).

* Corresponding author.
E-mail address: Patrick.Peplowski@jhuapl.edu (P.N. Peplowski).

0019-1035/$ - see front matter © 2013 Elsevier Inc. All rights reserved.
http://dx.doi.org/10.1016/j.icarus.2013.09.007

The Na/Si abundance ratio of 0.12 ± 0.01 reported by Evans et al. (2012) is an average value for Mercury's northern hemisphere and corresponds to 2.9 ± 0.1 wt% Na for an assumed Si abundance of 25 wt%. Here we present a new analysis of the GRS observations which reveals that the Na abundance varies spatially on Mercury. These measurements are limited to the northern hemisphere because of MESSENGER's eccentric orbit and high northern periapsis (Peplowski et al., 2011a, 2012).

2. Gamma-ray measurements

2.1. Na gamma-ray emission

Sodium is a stable, mono-isotopic (^{23}Na) element that emits gamma rays at characteristic energies when its nucleus is excited by galactic-cosmic-ray (GCR) induced neutrons. These neutrons are produced by spallation reactions within the top few meters of the regolith on airless or nearly airless bodies such as Mercury. There are two notable Na gamma rays, one with an energy of 440 keV that results from fast (energy $E_n > 0.4$ MeV) neutron inelastic scattering (n,n′γ) reactions, and another at 472 keV that results from thermal ($E_n < 0.2$ eV) neutron capture (n,γ) reactions. The relatively low energies of these two gamma rays means that only those produced within ~10 cm of the surface can escape to space at their full energy and be unambiguously identified by the GRS. An example GRS spectrum in the region of the 440-keV Na peak was given by Evans et al. (2012).

The 472-keV peak cannot be used to derive Na abundances on the surface of Mercury because of interference from the broad 478-keV peak that originates from (n,γ) reactions with ^{10}B in the large borated plastic anti-coincidence shield that surrounds the gamma-ray sensor. The 440-keV peak also suffers from an overlapping peak resulting from ^{69m}Zn decay (where the symbol m denotes a meta-stable state). ^{69m}Zn is a spallation product of the interaction of GCRs with the detector material. It was observed during interplanetary transfer and prior to each Mercury flyby (Goldsten et al., 2007) and is unrelated to gamma-ray emissions from Mercury. For the majority of MESSENGER's orbit (~11 out of 12 h during the primary mission), Mercury did not appreciably obscure the spacecraft-incident GCR flux (Evans et al., 2012). As a result, the GCR excitation source and consequent gamma-ray background count rate (^{69m}Zn half-life = 13 h) were effectively constant over MESSENGER's orbital period. Additionally, the lack of Na on the spacecraft means that there is no spacecraft-originating background to remove. This situation contrasts with that for most other (n,n′γ) gamma rays, which have spacecraft- and planet-originating components (Evans et al., 2012). Since the near-constant ^{69m}Zn peak is the only background contribution to the Na signal, the background was treated in the same manner as that used for the radioactive elements (Peplowski et al., 2011b, 2012). This treatment involves characterizing the count rate far from the planet (altitude >14,000 km) and subtracting it from the low-altitude measurements to determine the portion that originates from Mercury's surface.

In order to remove systematic variability associated with changes in the absolute GCR flux, gamma-ray measurements are frequently normalized to a known elemental abundance (e.g., Mars Odyssey GRS analysis, Boynton et al., 2007). Unlike the case for Mars, there is no ground-truth value for Mercury, but Si is a major element that has been shown to vary spatially much less than other major elements on Mercury (Peplowski et al., 2012), and MESSENGER GRS measurements have therefore previously been normalized to Si (Evans et al., 2012). Silicon has a strong (n,n′γ) line at 1779 keV that is used to calculate a Na/Si gamma-ray count-rate ratio. This count-rate ratio is converted to an abundance ratio with knowledge of the (n,n′γ) cross sections, detector efficiency, and a forward model to propagate the surface gamma-ray flux to the spacecraft. This process has been discussed in detail by Evans et al. (2012) and was used to determine the average Na/Si abundance ratio in the northern hemisphere (0.12 ± 0.01).

The GRS-measured Na abundance of Evans et al. (2012) is consistent with earlier inferences from ground-based mid-infrared spectroscopy for the presence of Na-bearing plagioclase feldspar on Mercury's surface, with compositions ranging from albite ($NaAlSi_3O_8$) with up to 5 wt% anorthite ($CaAl_2Si_2O_8$) to labradorite with 30–50 wt% albite (Sprague et al., 2007). Petrologic modeling of the composition of Mercury's crust from the surface elemental compositions determined from XRS (Weider et al., 2012) and GRS (Evans et al., 2012) measurements indicated that a substantial abundance of plagioclase (as much as 57%) may be present in the northern smooth plains (SP) unit (Stockstill-Cahill et al., 2012). As SP units on Mercury are located predominantly in the northern hemisphere (Denevi et al., 2013), spatially resolved measurements of Na from the GRS can be used to test the hypothesis that the SP units have higher abundances of Na, and by extension Na-rich plagioclase feldspar, than other areas on Mercury.

2.2. Na abundance within latitudinal bands

We have performed a new analysis of the Na peak using only low-altitude, southbound data in order to maximize the spatial resolution of the measurements. During MESSENGER's primary mission, the southbound portion of the spacecraft's orbit about Mercury was at lower altitudes than the northbound portion (e.g., Peplowski et al., 2012) and therefore permitted observations with superior spatial resolution. Note that the spatial resolution of the GRS measurements is approximately 1.5 times the altitude. Unfortunately, restricting the analysis to southbound data limits the total number of spatially resolved measurements that can be reported and also reduces their statistical significance. The data set is insufficient to create an abundance map, but it does allow for measurements to be distinguished by latitude within the northern hemisphere.

We binned the southbound GRS measurements into bands of width 15° in latitude. The Na/Si ratio was determined for each band following the procedure outlined in Section 2.1 and discussed in detail by Evans et al. (2012). The results for each latitude band are listed in Table 1, including their statistical uncertainties at one standard deviation (σ). Alternative latitude bands corresponding to measurements from 0°N to 60°N latitude and >80°N latitude are also included in Table 1. The latitude bin from 0°N to 60°N was processed separately and is not simply the average over the four 15°-wide bins. The purpose of including this latitude bin is to obtain a measure of the Na/Si content for mid- to equatorial latitudes with the highest possible statistical significance. The individual measurements for the 15°-wide latitude bins located at latitudes south of 60°N (Table 1) are each consistent with that derived from the latitude band from 0°N to 60°N (Na/Si = 0.107 ± 0.008) to within 1σ. This agreement suggests a more or less uniform abundance ratio in the mid-latitude and equatorial regions at the spatial resolution of the GRS measurements, so the ratio for the latitude band from 0°N to 60°N is therefore adopted as the equatorial abundance value.

The extreme north polar band (latitude >80°N) has a Na/Si abundance ratio of 0.20 ± 0.03, which is 3σ higher than the equatorial value and is therefore a statistically significant detection of higher Na/Si in the north. In order to estimate the absolute abundance of Na on the surface, we adopt a Si abundance of 25 wt%. This value is consistent with estimates based on the typical stoichiometry of major cations derived from MESSENGER XRS and GRS surface composition measurements (see the Supplementary

Table 1
Observed latitudinal variability of Na over the northern hemisphere of Mercury.

Latitude range	Average altitude (km)	Approximate spatial resolution[a] (km)	Na/Si abundance ratio	Na abundance (wt%)[b]
0–15°N	977	1500	0.115 ± 0.015	2.8 ± 0.4
15–30°N	646	1000	0.098 ± 0.016	2.4 ± 0.4
30–45°N	447	700	0.123 ± 0.019	3.0 ± 0.4
45–60°N	343	500	0.103 ± 0.018	2.5 ± 0.4
60–75°N	351	500	0.129 ± 0.019	3.2 ± 0.4
75–90°N	456	700	0.172 ± 0.020	4.2 ± 0.5
0–60°N			0.107 ± 0.008	2.6 ± 0.2
80–90°N			0.198 ± 0.030	4.9 ± 0.7

[a] The spatial resolution for an omnidirectional Gamma-Ray Spectrometer is approximated as 1.5 times the orbital altitude.
[b] Na abundance is calculated under the assumption of a constant Si abundance of 25 wt% across the surface (see Evans et al., 2012).

material of Lawrence et al. (2013)) and petrologic modeling of representative Mercury crustal compositions (Stockstill-Cahill et al., 2012). This Si abundance yields a Na abundance of 2.6 ± 0.2 wt% in the equatorial region and 4.9 ± 0.7 wt% in the north polar region (>80°N latitude). Although some of this variability could in principle be due to variations in Si, GRS data indicate that the relative Si abundance distribution across the surface varies by ⩽15% (Peplowski et al., 2012). Stochiometric analysis of Mercury crustal compositions suggests that Si varies by ∼10% between the major geochemical units sampled by the XRS (Supplementary material of Lawrence et al. (2013)). On the basis that Si variability is ∼10%, and because the GRS measurements show no indication of latitude-dependent variability in the Si gamma-ray signature (see Fig. 6 of Peplowski et al. (2012)), we conclude that the observed Na/Si variability is dominated by variations in the Na abundance.

3. Forward modeling

3.1. Modeling procedure

The coarse spatial resolution of the GRS-measured distribution of surface Na abundance with latitude (Table 1) prohibits the mapping of Na abundances on the scale of specific geologic units on the surface of Mercury. An intermediate step of comparing forward models of possible distributions with the measurements is required. We use a forward modeling procedure similar to that carried out for previous GRS (Peplowski et al., 2011a) and MESSENGER Neutron Spectrometer (Lawrence et al., 2011, 2013) analyses. These analysis techniques were initially developed for application to lunar nuclear spectroscopy data sets (e.g., Hagerty et al., 2006) and have been validated against independent, high-spatial-resolution measurements (e.g., Glotch et al., 2011). Our forward models yield maps produced from hypothetical distributions of the Na/Si abundance ratio across Mercury's northern hemisphere. These maps are used to create model-based Na/Si latitude profiles that are compared with the GRS measurements (Table 1) to test the validity of the underlying assumptions.

The forward modeling procedure begins with an assumed spatial distribution for the Na/Si abundance ratio. For example, Section 3.2 presents the hypothesis that Na/Si is higher in the smooth plains units than it is in the intercrater plains and heavily cratered terrain. The assumed Na/Si distribution maps have a spatial resolution (∼10 km) that is significantly higher than the spatial resolution of the GRS measurements (500–1500 km, Table 1). As a result, these maps must be convolved with the altitude-dependent spatial response of the detector to produce the spatial distribution that would be observed by the GRS. Examples of these smoothed maps are shown in Fig. 1, and the inputs for these maps are discussed in Sections 3.2 and 3.3. Because of MESSENGER's eccentric orbit about Mercury, the spatial resolution of the GRS is constantly changing. This variability necessitated the production of multiple maps for each Na/Si distribution hypothesis, each corresponding to a different altitude-dependent spatial resolution. The maps were combined to form a single map for each Na/Si distribution hypothesis with the correct latitude-dependent spatial resolution (Fig. 1). Specifically, the full map (0−90°N latitude) is produced from the 1500-km spatial resolution map for 0−15°N latitude, the 1000-km spatial resolution map for 15−30°N latitude, the 700-km spatial resolution map for 30−45°N and 75−90°N latitude, and the 500-km spatial resolution map for 45−75°N latitude. These latitude ranges and spatial resolutions match those of the GRS measurements (see Table 1). The resulting maps (Fig. 1) approximate the assumed Na/Si distributions that would be seen by the GRS, although we have approximated the smoothly varying spatial resolution across the surface with the quantized values listed in Table 1.

In order to test the validity of our hypothesized Na/Si distributions, we compared the forward-model-derived latitude distributions with the GRS measurements. This comparison was made by taking the average Na/Si abundance ratio in the modeled maps (Fig. 1) from each latitude band as defined by the GRS measurements. The resulting modeled Na/Si latitude profiles were directly compared with the corresponding GRS-derived Na/Si abundance ratios as a test of the assumed distribution. This process was iterated until the two end-member hypothetical Na/Si distributions were found that are consistent with the one-standard-deviation errors of the GRS measurements (e.g. Fig. 2). In Sections 3.2 and 3.3 we discuss the results of these modeling efforts for three possible distributions of surface Na/Si abundance ratio. We interpret the implications of these models with respect to our current understanding of the geochemistry of Mercury's surface in Section 4.

3.2. Models with enhanced Na in the smooth plains

The Na abundance measurements binned by latitude (Table 1) reveal a high Na abundance at high northern latitudes (>75°N), a region that is dominated by a large expanse of volcanic smooth plains (Head et al., 2011). Petrologic modeling by Stockstill-Cahill et al. (2012) of the elemental abundance measurements of the northern plains made with the MESSENGER XRS (Weider et al., 2012) and GRS (Evans et al., 2012), specifically a Na value of 3 wt%, indicate that this unit may contain a high abundance of feldspars that are Na-rich (see Section 2.2). In contrast, the older intercrater plains and heavily cratered terrain (IcP-HCT) that surround the northern plains typically have higher Mg/Si ratios and lower Al/Si ratios, indicative of lower feldspar abundances (Weider et al., 2012). These observations led to the hypothesis that Na abundances are generally higher in smooth plains on Mercury than in the IcP-HCT. That smooth plains elsewhere on Mercury may be compositionally similar to the northern smooth plains is supported by the observation that most SP units have spectral characteristics that are similar to the northern plains (Denevi et al., 2013), as well

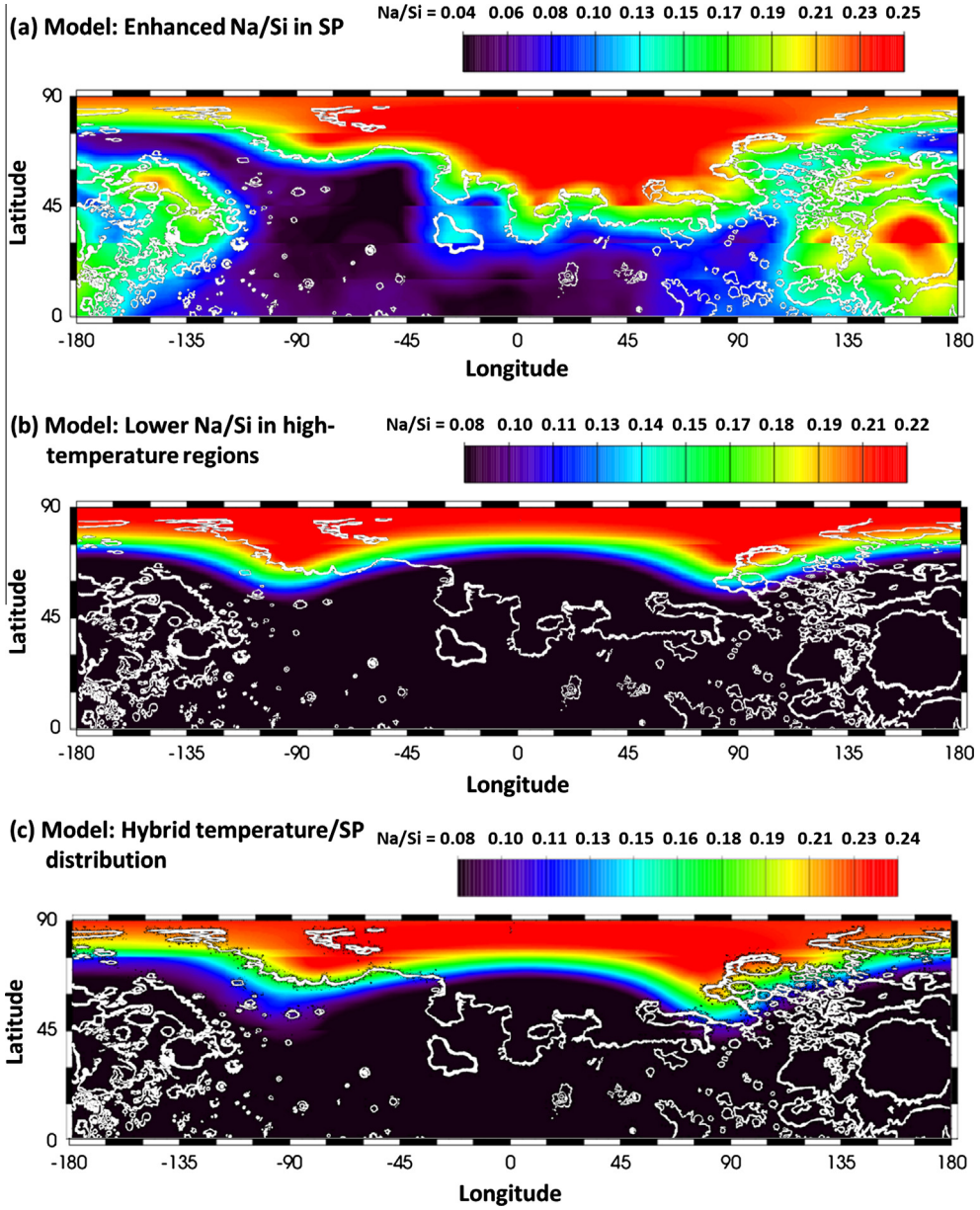

Fig. 1. Example outputs from the forward model for a given distribution of Na/Si abundance ratio. (a) For a scenario with a Na/Si abundance ratio of 0.250 assigned to the smooth plains (SP) units (white outlines) as identified by Denevi et al. (2013) and a ratio of 0.040 assigned to all areas outside of the SP units. (b) For a scenario with a Na/Si abundance ratio of 0.220 assigned to regions where the maximum temperature at a depth of 7 cm never exceeds 400 K and a ratio of 0.085 to regions where temperature at that depth exceeds 400 K. (c) For a scenario with a Na/Si abundance ratio of 0.243 assigned to the smooth plains (SP) units and a ratio of 0.120 assigned to all areas outside of the SP units, except that in regions with a maximum near-surface temperature greater than 400 K, the Na/Si abundance was reduced to 0.080 to reflect thermal depletion of moderately volatile Na. Discontinuities in the maps originate from the different spatial resolutions applied to each latitude band, which were selected to match the values listed in Table 1. The modeled results were binned by latitude to match the observations and subsequently compared with the GRS measurements (e.g., Figs. 2 and 4) Caloris basin is the large (~1550-km diameter) near-circular feature centered at ~30° N latitude and ~170° E longitude.

as by the similarities in the abundances measured by XRS of the other major rock-forming elements in the northern plains and the smooth plains interior to the Caloris basin (Weider et al., 2012). SP units cover approximately 27% of Mercury's surface and are found mainly at mid- and high-northern latitudes (Denevi et al., 2013). The distribution of smooth plains thus provides a possible explanation for our observation of higher Na abundances at higher latitudes.

The forward modeling procedure (Section 3.1) was used to test the hypothesis that smooth plains units have higher Na abundances than other terrains on Mercury. Different Na/Si abundance ratios were assigned to the SP and IcP-HCT units, the locations of which were taken from the global mapping by Denevi et al. (2013). The distributions of SP and IcP-HCT units were convolved with the altitude-dependent spatial response of the GRS, binned into latitude bands as was done with the GRS data, and finally compared with the measurements. An example output of this forward model is shown in Fig. 1a. The forward-modeled abundance ratios for the two units were iterated until the two extreme values were found that are consistent with the 1σ errors of the GRS measurements (dashed curves in Fig. 2). The comparison shows that this hypothesis is consistent with the data for Na abundances of 4.2–6.2 wt% in SP units and 1.0–2.9 wt% in the IcP-HCT areas (for an assumed Si abundance of 25 wt%; see Section 2). Despite the general agreement, the model overestimates the Na/Si ratio for latitudes between 45°N and 75°N compared with the observations,

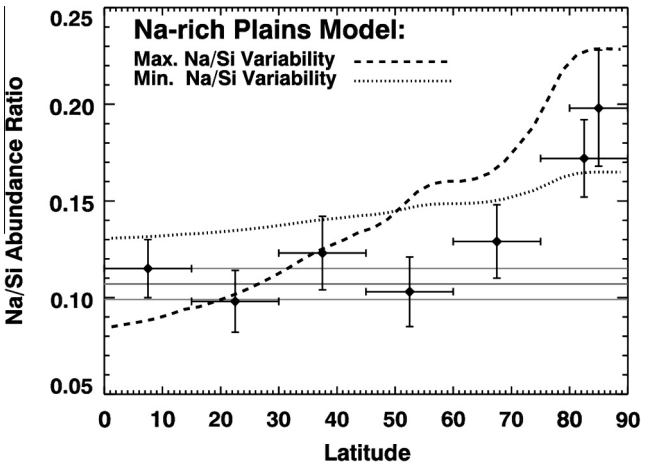

Fig. 2. Na/Si weight ratios and one-standard-deviation statistical uncertainty versus latitude as measured by the MESSENGER GRS. Results from the 15°-wide latitude bands, as well as the 80–90°N band, are included. The mean value and one-standard-deviation errors for the 0–60°N band are also shown as thick and thin gray lines, respectively. The predicted Na/Si abundance distributions for the model in which the smooth plains have higher Na/Si values than surrounding terrain (Section 3.2, Fig. 1a) are shown as dashed lines. The two extreme surface Na/Si distributions correspond to values of (long dashed line) 0.25 and 0.04 and (short dashed line) 0.17 and 0.12 for the SP and IcP-HCT units, respectively.

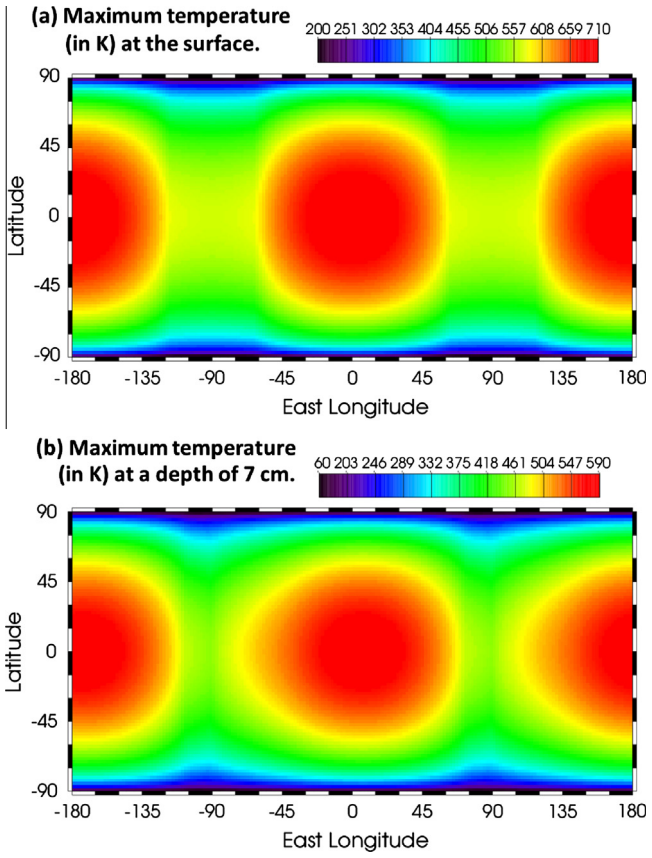

Fig. 3. Modeled maximum temperatures at (a) Mercury's surface and (b) at a depth of 7 cm, from the work of Vasavada et al. (1999). These depths were chosen on the basis that they bound the depth range over which the GRS measurements are sensitive to Na gamma rays. The hot poles, located at the equator at 0° and 180° longitudes, are clearly observed in both maps.

suggesting that another process may be contributing to the observed Na distribution. These latitudes include the upper portion of the Caloris basin, and the southern extension of the northern smooth plains deposits (between longitudes of -60° and 115°E). These areas hosts interior SP deposits that increase the modeled Na/Si ratio at mid-latitudes in a manner that is not apparent in the GRS measurements.

3.3. Models with thermal redistribution of Na

As a result of Mercury's 3:2 spin–orbit resonance, coupled with it's near-zero obliquity and large orbital eccentricity, the maximum surface and near-surface temperatures vary markedly across the surface. This variability is shown in Fig. 3, which illustrates modeled maximum temperatures derived following the procedure of Vasavada et al. (1999). Maximum temperatures are shown both at the surface and at a depth of 7 cm, locations that bound the range of depths to which Na gamma-ray measurements are sensitive. Two points on the equatorial surface at 0° and 180° longitude are directly subsolar during alternating perihelia and therefore experience the highest surface temperatures (>600 K). These locations, known as Mercury's hot poles, are clearly illustrated in Fig. 3. Temperatures in the polar regions are substantially lower, with maximum values below 350 K and as low as ~60 K in permanently shadowed regions (Paige et al., 2013).

Sodium is a moderately volatile lithophile element, and its distribution may be modified by the high temperatures of Mercury's surface. This inference follows from the findings of Peplowski et al. (2012), who observed an anti-correlation between the abundance of the similarly volatile element K and the maximum surface temperature. That observation was interpreted as possible evidence for diffusive loss of K from alkali feldspars in areas of high maximum surface temperature and possible re-deposition in areas of lower maximum surface temperature. This conclusion is supported by the work of Madey et al. (1998), who compiled experimental data on adsorption and desorption of alkalis on oxide surfaces and concluded that thermal desorption would rapidly deplete Mercury's equatorial regions of alkali elements. A similar mechanism has been invoked as a possible source process for Mercury's neutral exosphere (Leblanc and Johnson, 2003, 2010; Leblanc et al., 2007). Diffusive loss can also occur for Na, and because of it's smaller ionic radius compared to K, the diffusion of Na in alkali feldspars is 2–3 orders of magnitude faster than for K (Kasper, 1975; Giletti and Shanahan, 1997). Na-rich feldspars are expected to be present on Mercury's surface on the basis of the petrologic modeling of Stockstill-Cahill et al. (2012) (see Section 2.2), although Na may also be present in other minerals such as sulfides. Grains of ~10 μm size in the regolith would efficiently lose Na over ~1 Gy at temperatures above ~400 K, whereas potassium loss would occur only at temperatures above ~475 K. Comminuted alkali feldspars in the regolith of Mercury would therefore experience Na loss over a broader area of the planet than for K.

Mercury's polar regions are sufficiently cold that they would be expected both to retain their original inventories of Na and K and in the presence of thermally driven mobilization they potentially serve as cold traps for Na and K volatilized from the hotter equatorial and mid-latitude regions (e.g., Yan et al., 2006). If redistribution is not a major process, then the northernmost measurements may represent the original Na abundance of the surface in this region, which is dominated by the large SP unit (Head et al., 2011; Denevi et al., 2013). The elemental composition of this unit was measured by the XRS (Weider et al., 2012) and found to be consistent with higher abundances of alkali feldspars (see Sections 2.2 and 4). The distribution of Na south of 60°N, in contrast, may have been irreversibly modified by temperature-driven mobilization. Loss of Na would be expected to have been particularly strong near Mercury's hot poles.

3.3.1. Thermal redistribution

On the grounds that Na should be mobilized on Mercury because of the high temperatures experienced by portions of the surface, we hypothesize that the GRS-measured Na/Si distribution may be the result of thermal depletion and re-deposition. Testing this hypothesis requires knowledge of the maximum surface temperatures to the depth of the gamma-ray measurements (<10 cm for a 440 keV gamma ray). We used the maps of maximum temperature at depths of 0 and 7 cm given in Fig. 3. This temperature map formed the basis for a two-component map of Mercury's surface corresponding to regions for which maximum temperatures at 7 cm depth were either above or below a threshold of 400 K. As discussed above, laboratory experiments suggest that 400 K is the temperature at which Na in alkali feldspars begins to diffuse from grains. This model is based on the premise that the current Na distribution is determined solely by thermal effects; any initial variability that may have been present as a result of compositional variations is assumed to have been overprinted by the redistribution. Following the forward modeling procedure presented in Section 3.1, Na/Si abundance ratios were assigned to the two regions and compared with GRS measurements. An example output of the forward model is shown in Fig. 1b. The forward-modeled abundance ratios for the two units were iterated until the two extreme values were found that are consistent with the 1σ errors of the GRS measurements. The allowed Na abundances are 4.2–5.4 wt% in the cooler (<400 K maximum temperature at 7 cm depth) regions and 2.1–3.2 wt% in the warmer (>400 K maximum temperature) equatorial regions. Although not illustrated here, the results are nearly identical to those of the next model (Section 3.3.2), the results of which are detailed in Fig. 4.

3.3.2. Thermal redistribution with underlying compositional variability

Although thermal mobilization alone can account for the GRS-measured Na/Si distribution, there is evidence from the XRS and petrologic modeling of elemental concentrations that there are underlying variations in the abundance of feldspar, and by inference Na, across Mercury's surface. We therefore develop a final hypothesis that the observed Na/Si distribution results from a combination of elemental abundance variability on the surface and thermal mobilization. We began with the assumptions adopted in Section 3.2, specifically that Na is higher in the SP units than in the IcP-HCT. We also invoked the assumption from Section 3.3.1 that Na is lowest in regions that experience maximum near-surface temperatures above 400 K. This hypothesis results in a three-component abundance map. Na/Si abundances were assigned to the three regions, the distribution was convolved with the altitude-dependent spatial resolution of the GRS, the results were binned into the same latitude bands as the GRS measurements, and finally the results were compared with the measured Na/Si distribution (Table 1). An example output of the forward model is shown in Fig. 1c. The forward-modeled abundance ratios assigned to each component of the map were iterated until the maximum and minimum values consistent with the 1σ errors in the GRS measurements were found. The results are shown in Fig. 4, where the endpoints of these ranges correspond to the dashed curves. Although the results of the first hypothesis (Section 3.2, Fig. 2) alone were marginally consistent with the measurements, the addition of secondary alteration via thermal modification (Fig. 3) greatly improves the fit to the data, particularly in the mid-latitude region. The allowed Na abundances are 4.2–6.0 wt% in the SP (where temperature at 7 cm depth is less than 400 K), 2.9–3.2 wt% in the IcP-HCT (where temperature at 7 cm depth is less than 400 K), and 2.0–3.2 wt% in regions where the maximum surface temperature at 7 cm depth exceeds 400 K.

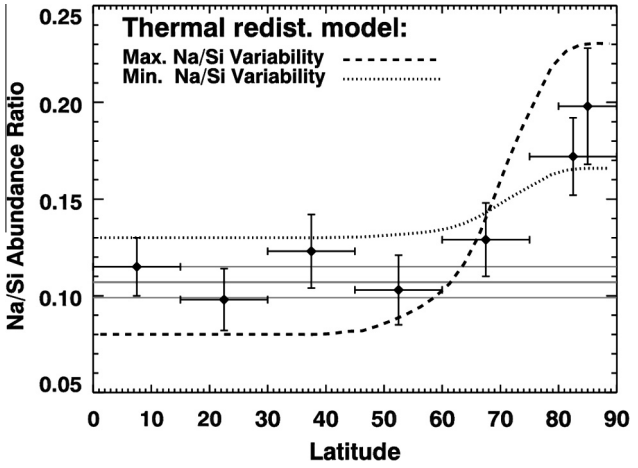

Fig. 4. Comparisons of measured and modeled Na/Si weight ratios versus latitude. The measurements and one-standard-deviation statistical uncertainties are identical to those detailed in Fig. 2. The predicted Na/Si abundance distributions (dashed lines) are for the model in which there are different Na/Si abundances for the SP and IcP-HCT as well as depletion of Na from the warmer (>400 K) equatorial regions (Section 3.3.1, Fig. 1c). The two extreme surface distributions correspond to Na/Si abundance ratio values of (long dashed line) 0.243, 0.120, and 0.080 and (short dashed line) 0.170, 0.130, and 0.130 for the SP units (maximum temperature at 7 cm depth <400 K), IcP-HCT (maximum temperature at 7 cm depth <400 K), and hotter regions (maximum temperature at 7 cm depth >400 K), respectively.

4. Implications for the geochemistry of Mercury's surface

4.1. Comparison to previous measurements

Measurements of Mercury's surface composition by the MESSENGER XRS (Weider et al., 2012) have demonstrated that the northern hemisphere contains at least two compositionally distinct units. One of those units corresponds approximately to the northern SP unit identified by Head et al. (2011) and mapped by Denevi et al. (2013). This unit has major element abundance ratios (e.g., higher Al/Si, lower Mg/Si) that are suggestive of a higher feldspar content than that of the surrounding IcP-HCT terrain (Stockstill-Cahill et al., 2012). Although anorthite ($CaAl_2Si_2O_8$) is expected to dominate, the alkali feldspars albite ($NaAlSi_3O_8$) and K-rich ($KAlSi_3O_8$) may also be present, and their abundances are predicted to increase as the abundance of elemental Na increases (Stockstill-Cahill et al., 2012). The observation that the potentially feldspar-rich northern SP unit also corresponds approximately to the region with the highest measured K abundances (~2000 ppm; Peplowski et al., 2012) supports this prediction, although this measured K abundance alone cannot account for the amount of feldspar inferred from the measured Al abundance. As a result, the feldspar content of the northern SP must include non-K-rich feldspar varieties as well. The average northern hemisphere Na abundance (~2.9 wt%) reported by Evans et al. (2012) provides sufficient Na to make up the difference, and the petrologic modeling of Stockstill-Cahill et al. (2012) indicated that up to 57% plagioclase, including at least 17% albite, is possible within this SP unit on the basis of the Evans et al. (2012) Na value.

Our discovery of higher Na abundances at the northernmost latitudes (>75°N), an area that is dominated by the northern SP unit, strengthens the case for high abundances of alkali feldspars in this region. Since the majority of the SP units have similar abundances of other elements and similar spectral characteristics to the northern SP unit (Denevi et al., 2013), it can be inferred that other SP units may be comparable in Na abundance, at least prior to any thermal loss. This scenario corresponds to the hypothesis

Table 2
Results of crystallization modeling[a] at the last temperature step for each composition.

Component (wt.%)	NVP with 0.2% Na	NVP with 3.4% Na	NVP with 4.7% Na
Sulfides[b]	2	2	2
Liquid	5	0	1
Olivine	2	8	27
	Fa_{8}	Fa_{8}	Fa_{6-11}
Orthopyroxene	41	31	–
	$Wo_{0-1}En_{87-93}Fs_{7-15}$	$Wo_{2-3}En_{87-90}Fs_{9-10}$	
Clinopyroxene	–	<1	10
		$Wo_{43}En_{52}Fs_{5}$	$Wo_{44-57}En_{38-51}Fs_{4-5}$
Plagioclase	24	58	61
	$An_{83-90}Or_{0-1}$	$An_{36-83}Or_{0-1}$	$An_{14-44}Or_{0-2}$
Spinel	5	1	1
	$C_{18-57}U_{0-2}S_{42-82}$	$C_{33-59}U_{0-16}S_{40-62}$	$C_{30-60}U_{0-19}S_{40-62}$
Quartz (polymorph)	22	–	–
Corundum	1	–	–
Rhombic oxide	–	1	0
		$Gk_{60-61}Ilm_{34-35}Py_{4-5}$	$Gk_{58-63}Ilm_{35-41}Py_{1-2}$

[a] Final component abundances are rounded to the nearest percent; dashes indicate components that did not appear in the crystallization model. NVP denotes northern volcanic plains.

[b] Sulfide ($Mg_{0.75}Ca_{0.25}S$) amount was removed prior to MELTS modeling following Stockstill-Cahill et al. (2012). Mineral compositions represent the range displayed during modeled crystallization as shown in Fig. 5. Orthopyroxene and clinopyroxene compositions are denoted in terms of the wollastonite (Wo), enstatite (En), and ferrosilite (Fs) proportions. Plagioclase compositions are denoted by the anorthite (An) and orthoclase (Or) proportions. Spinel compositions are denoted by their chromite (C), ulvöspinel (U), and spinel (S) proportions. Rhombic oxide end-members are denoted by geikielite (Gk), ilmenite (Ilm), and pyrophanite (Py).

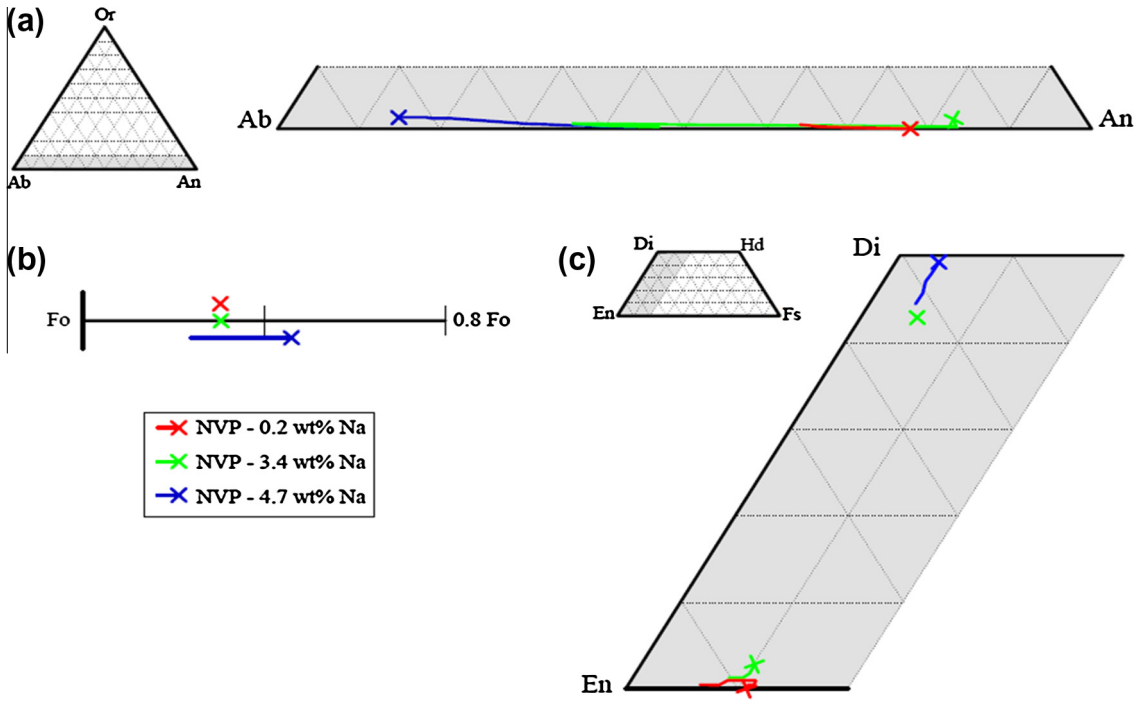

Fig. 5. Mineral compositions predicted from crystallization modeling of magmas matching the elemental composition of Mercury's northern volcanic plains (NVP) for three different assumed Na abundances for (a) feldspars (Ab = albite, An = anorthite, Or = orthoclase), (b) olivine (Fo = forsterite), and (c) pyroxenes (Di = diopside, Hd = hedenbergite, En = enstatite, and Fs = ferrosilite). The albite (Na-rich) to anorthite (calcium-rich) portion of the feldspar ternary is shown as an inset in (a). The range of the olivine plot in (b) is from Fa_{100} to Fa_{80}. The Mg-rich portion of the full pyroxene quadrilateral is shown as an inset in (c). Compositions are derived from modeled compositions that are S-free. Lines indicate crystallization trends for a given mineral, with the "x" indicating the final or only mineral composition crystallized.

examined in Section 3.2, and the modeled abundance ratios from this scenario are broadly consistent with the GRS measurements (see Fig. 2). The possibility that thermal depletion of Na near the hot poles also contributes to the distribution (Section 3.3) notably improves the fit to the data (Fig. 4). We therefore conclude that our measured Na distribution supports the statements of Weider et al. (2012) and Stockstill-Cahill et al. (2012) that the SP units contain higher abundances of alkali feldspars than the IcP-HCT, and that the measured equatorial Na abundances are consistent with intrinsically lower values within the IcP-HCT and depletion via thermal modification similar to that proposed for K by Peplowski et al. (2012).

4.2. Petrologic modeling with high Na abundances

Stockstill-Cahill et al. (2012) used the MELTS program (Ghiorso and Sack, 1995; Asimov and Ghiorso, 1998) to explore the petrogenesis of Mercury's crust. Inputs to their modeling included XRS- and GRS-measured surface compositions, including the spatially resolved measurements of the SP and IcP-HCT compositions

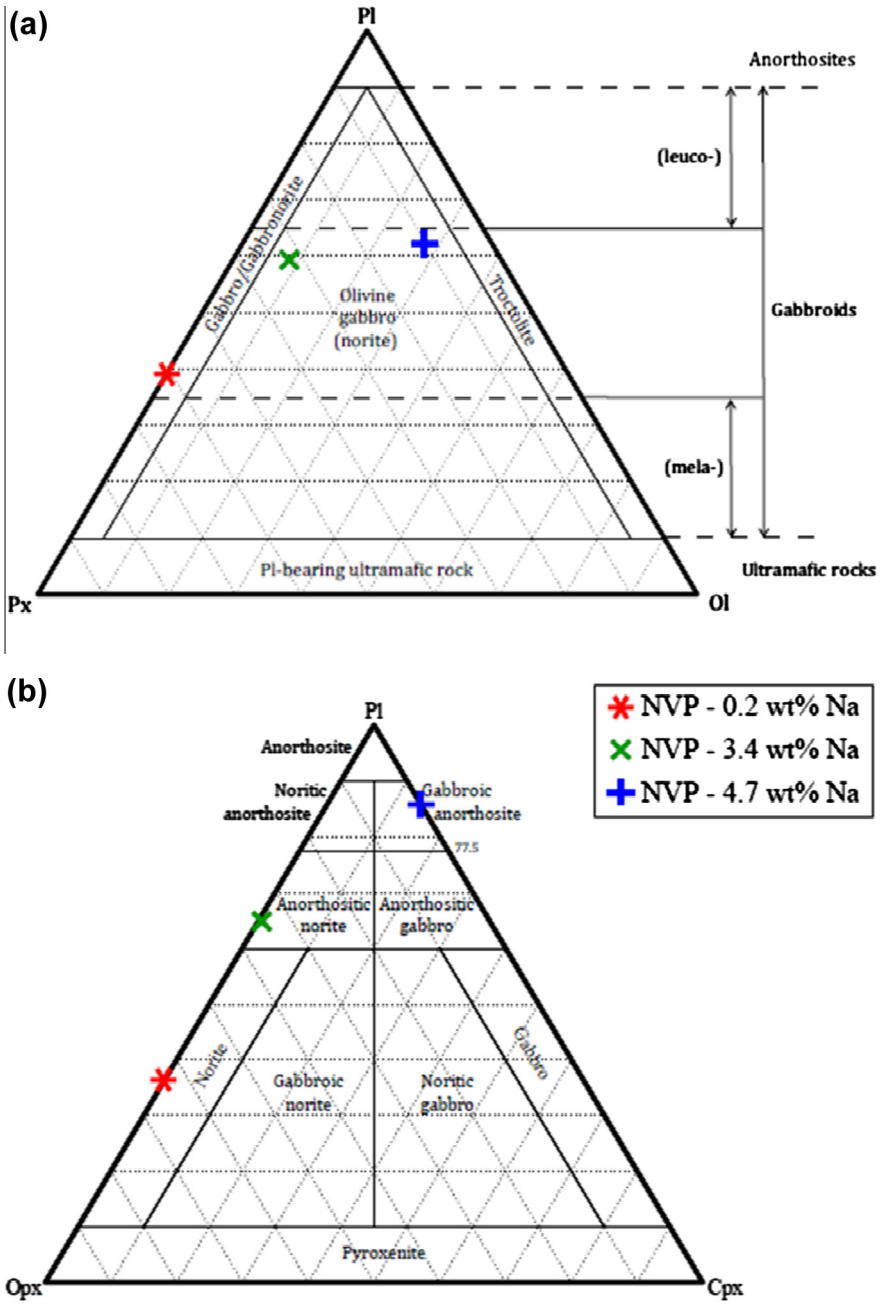

Fig. 6. Rock compositions predicted from crystallization modeling of magmas matching the elemental composition of NVP for three different assumed Na abundances, plotted on standard rock classification diagrams. (a) Plagioclase–pyroxene–olivine (Pl–Px–Ol) ternary diagram. (b) Plagioclase–orthopyroxene–clinopyroxene (Pl–Opx–Cpx) ternary diagram. Compositions are derived from modeled compositions that are S-free.

of Weider et al. (2012) and the average northern hemisphere values of Evans et al. (2012). The models were constructed under the assumption that highly reducing conditions, fO_2 values of 2.6–6.3 $\log_{10}$ units below the iron-wüstite (IW) buffer, governed Mercury's early magmatic history. These fO_2 values are supported by recent estimates of Mercury's oxygen fugacity as derived from MESSENGER XRS measurements of S and Fe (McCubbin et al., 2012; Zolotov et al., 2013). Although MELTS has been shown to produce poor matches for lunar basalts at lower oxygen fugacities (Slater et al., 2003; Thompson et al., 2003), likely because the code was calibrated for terrestrial (i.e., more oxidizing) conditions, Stockstill-Cahill et al. (2012) found that for the Mercury's compositions they modeled the results were largely independent of the fO_2 value as long as it was below the IW buffer. As a result, the fO_2 values for the models were held at the IW buffer.

Stockstill-Cahill et al. (2012) noted that among the moderately volatile elements (i.e., Na, K, S), Na is the only one for which the abundance strongly influences the proportion of major phases (plagioclase, mafic silicates) that crystallize. Higher Na abundances during crystallization produce more plagioclase, and such plagioclase has a higher albite content. Because albite includes more Si and less Al than anorthite, higher Na abundances favor the crystallization of relatively Si-poor olivine ($(Mg,Fe)_2SiO_4$) over orthopyroxene ($(Ca,Mg,Fe)_2Si_2O_6$). We have extended the MELTS modeling of Stockstill-Cahill et al. to include the higher Na abundances we have observed in the northern polar region. The results

are shown in Table 2 and Fig. 5, and detailed outputs from the modeling are given in the Supplementary online material. For this modeling it was assumed that our measured Na abundances are from co-genetic material that was present during the crystallization of the magmas and not from a volatile overprinting that resulted from mobilization of Na.

Our models indicate that when the Na abundance increases from low (0.24 wt%) to moderate (3.4 wt%) to high (4.7 wt%) levels, the feldspar compositions shift to more albitic compositions (Fig. 5a) and the overall plagioclase abundance more than doubles (Table 2). Although the overall mafic silicate abundance remains constant (38% for low, 43% for moderate, 37% for high), there is a shift in the ratio of orthopyroxene to olivine (41%:2% for low, 30%:8% for moderate, 0%:27% for high) and the appearance of clinopyroxene (0% for low, <1% for moderate, 10% for high) (Table 2 and Fig. 5b and c). The appearance of clinopyroxene at high Na abundances is driven by the availability of Ca resulting from the transition of the plagioclase content from anorthite toward albite. The doubling of the plagioclase content resulting from the increase in Na abundance from 0.2 to >3 wt% changes the nature of the crust from a gabbronorite to an olivine gabbronorite, as given by the plagioclase–pyroxene–olivine ternary classification (Fig. 6a), and from a norite to an anorthositic norite to a gabbroic anorthosite, in terms of the plagioclase–olivine–clinopyroxene ternary classification (Fig. 6b).

Our prediction that the north polar region may be dominated by Na-rich feldspars (Table 2) must be reconciled with the inference that the dominant geologic unit in this region, a large expanse of volcanic plains, was formed by the geologically rapid emplacement of high-temperature, low-viscosity flood lavas (Head et al., 2011). Viscosities calculated for our modeled compositions using the method of Shaw (1972) produce fairly low values for both the liquids (0.43–6.92 Pa s) and partially crystallized liquids (73.5–80.0 Pa s). As the Na content of the material increases, the liquid viscosity decreases. With a mean crystal diameter of 1 mm and 50% crystallization, the most Na-rich composition has a viscosity of the liquid plus crystal of only 73.5 Pa s, which is lower than that of a typical terrestrial basaltic magma (at least 100 Pa s) (Basaltic Volcanism Study Project, 1981). Because of their low viscosities, these lavas would have been fluid, forming thin, laterally extensive units that flowed around topographic highs. This conclusion is consistent with the observation of numerous features indicative of highly fluid lavas (e.g., embayments, kipukas, lava channels, flow margins and flow fronts) in the northern volcanic plains and surrounding areas (Head et al., 2011; Byrne et al., 2013).

5. Conclusions

MESSENGER GRS measurements have demonstrated that the abundance of Na varies over the surface of Mercury. At the 300−1000 km spatial resolution of the GRS measurements and within the broad latitude bands used in this study, Na is approximately uniform southward of 60°N (Na/Si = 0.11 ± 0.01, Na ≈ 2.6 wt%) and is higher at high northern latitudes (>75°N). The maximum Na/Si weight ratio of 0.20 ± 0.03 (Na ≈ 5 wt%) is observed poleward of 80°N. This latitude band primarily samples the large area of northern smooth plains (Head et al., 2011), a unit known from XRS measurements to be compositionally distinct (Weider et al., 2012) from older surrounding terrain. This correspondence led to the development of the hypothesis that Na is higher in smooth plains units than in the surrounding intercrater plains and heavily cratered terrain. Forward modeling revealed that this hypothesis is consistent with the GRS measurements. The agreement between the models and measurements is improved when secondary modification of Na via thermal depletion is included. We tested a specific model of thermal depletion in which regions where the maximum near-surface temperature exceeds 400 K experience a loss of Na. This model is consistent with similar observations of the distribution of K (Peplowski et al., 2012) as well as expectations from laboratory measurements of Na diffusion in alkali feldspars (Kasper, 1975; Giletti and Shanahan, 1997). We conclude that a combination of high-Na smooth plains units and thermal modification can match the measured Na distribution. This result confirms previous indications from elemental abundance measurements and petrological modeling that the smooth plains units should contain higher abundances of Na-rich feldspars than are present within the IcP-HCT units (Weider et al., 2012; Stockstill-Cahill et al., 2012). Thermal modification alone can also account for the observed Na distribution, but that hypothesis cannot account for the XRS-derived inference of higher feldspar content in the SP or the petrologic modeling.

These findings have implications for the source processes for neutral Na atoms in Mercury's exosphere. Since its discovery in 1985 (Potter and Morgan, 1985), exospheric Na has been extensively studied. Its sources and sinks are related to a complex set of interactions between Mercury's surface and solar radiation, the solar wind, the micrometeoroid influx, the interplanetary magnetic field, and the magnetosphere (see Domingue et al., 2007, and references within). Thermal desorption, which has been suggested here as a possible mechanism for modifying the surface Na distribution to match observations (Section 3.3), was earlier considered as a possible source mechanism of the Na exosphere (Leblanc and Johnson, 2003, 2010; Leblanc et al., 2007).

The possibility of linking spatial variations in the characteristics of the exosphere to variations in Na abundances on the surface was proposed by Sprague et al. (1997, 1998). If such a link can be made, then Earth-based observations of Mercury's neutral Na exosphere could provide additional constraints on our modeled surface compositions. For example, Schleicher et al. (2004) and Potter et al. (2013) identified peaks in the neutral Na exosphere over both poles. If these peaks are due to enhancements in the surficial abundance of Na in the polar regions, then this would seem to support the thermal redistribution model and not the hypothesis of higher Na abundances in the SP, as the smooth plains units in the southern polar region are markedly smaller in total area than those found in the north (Denevi et al., 2013). However, low spatial resolution XRS measurements of south polar regions show lower Mg/Si and higher Al/Si ratios than are observed in equatorial regions (Nittler et al., 2011), with compositions overlapping those of the SP (Weider et al., 2012). Thus, crustal materials in the south polar regions may have a composition similar to that of the northern SP units, including high Na-rich feldspar abundances, despite the different morphology. Moreover, comparisons between the exosphere and surface composition are complicated by current uncertainties in exospheric source processes (e.g., Killen et al., 2004; Mura et al., 2009). The polar enhancements, for instance, may reflect different charged particle environment within the polar cusp regions (e.g. Vervack et al., 2010; Burger et al., 2010) rather than variations in surface composition. Given these uncertainties, we conclude that the Na exosphere measurements do not provide a direct constraint on our modeled surficial Na distributions. Further modeling of the exosphere that incorporates the GRS-measured distribution of Na on the surface may provide a more complete understanding of the physical mechanisms responsible for producing Mercury's neutral Na exosphere. Such modeling should be complemented by ongoing measurements of the exosphere by ground-based observers and MESSENGER, as well as by future observations to be made by the BepiColombo spacecraft of the European Space Agency and Japan Aerospace Exploration Agency (Benkhoff et al., 2010).

Acknowledgments

We thank the entire MESSENGER team for their invaluable contributions to the development and operation of the MESSENGER spacecraft. The MESSENGER mission is supported by the NASA Discovery Program under contracts NAS5-97271 to The Johns Hopkins University Applied Physics Laboratory and NASW-00002 to the Carnegie Institution of Washington. LGE acknowledges support from the MESSENGER Participating Scientist Program. We thank David Paige for providing the modeled Mercury surface temperatures. We also thank two anonymous reviewers for providing constructive comments that improved the manuscript.

Appendix A. Supplementary material

Supplementary data associated with this article can be found, in the online version, at http://dx.doi.org/10.1016/j.icarus.2013.09.007.

References

Asimov, P.D., Ghiorso, M.S., 1998. Algorithmic modifications extending MELTS to calculate subsolidus phase relations. Am. Mineral. 83, 1127–1131.

Basaltic Volcanism Study Project, 1981. Basaltic Volcanism on the Terrestrial Planets. Pergamon, New York. 1286pp.

Benkhoff, J. et al., 2010. BepiColombo – Comprehensive exploration of Mercury: Mission overview and science goals. Planet. Space Sci. 58, 2–20.

Boynton, W.V. et al., 2007. Concentration of H, Si, Cl, K, Fe, and Th in the low- and mid-latitude regions of Mars. J. Geophys. Res. 112, E12S99. http://dx.doi.org/10.1029/2007JE002887.

Burger, M.H. et al., 2010. Monte Carlo modeling of sodium in Mercury's exosphere during the first two MESSENGER flybys. Icarus 209, 63–74. http://dx.doi.org/10.1016/j.icarus.2010.05.007.

Byrne, P.K. et al., 2013. An assemblage of lava flow features on Mercury. J. Geophys. Res. Planets 118, 1303–1322. http://dx.doi.org/10.1002/jgre20052.

Denevi, B.W. et al., 2013. The distribution and origin of smooth plains on Mercury. J. Geophys. Res. Planets 118, 891–907. http://dx.doi.org/10.1029/2012JE004295.

Domingue, D.L. et al., 2007. Mercury's atmosphere: A surface-bounded exosphere. Space Sci. Rev. 131, 161–186. http://dx.doi.org/10.1007/s11214-007-9260-9.

Evans, L.G. et al., 2012. Major-element abundances on the surface of Mercury: Results from the MESSENGER Gamma-Ray Spectrometer. J. Geophys. Res. Planets 117, E00L07. http://dx.doi.org/10.1029/2012JE004178.

Ghiorso, M.S., Sack, R.O., 1995. Chemical mass transfer in magmatic processes. IV. A revised and internally consistent thermodynamic model for the interpolation and extrapolation of liquid-solid equilibria in magmatic systems at elevated temperatures and pressures. Contrib. Mineral. Petrol. 119, 197–212. http://dx.doi.org/10.1007/BF00307281.

Giletti, B.J., Shanahan, T.M., 1997. Alkali diffusion in plagioclase feldspar. Chem. Geol. 139, 3–20. http://dx.doi.org/10.1016/S0009-2541(97)00026-0.

Glotch, T.D. et al., 2011. The Mairan domes: Silicic volcanic constructions on the Moon. Geophys. Res. Lett. 38, L21204. http://dx.doi.org/10.1029/2011GL049548.

Goldsten, J.O. et al., 2007. The MESSENGER Gamma-Ray and Neutron Spectrometer. Space Sci. Rev. 131, 339–391. http://dx.doi.org/10.1007/s11214-007-9262-7.

Hagerty, J.J., Lawrence, D.J., Hawke, B.R., Vaniman, D.T., Elphic, R.C., Feldman, W.C., 2006. Refined thorium abundances for lunar red spots: Implications for evolved, nonmare volcanism on the Moon. J. Geophys. Res. 111, E06002. http://dx.doi.org/10.1029/2005JE002592.

Head, J.W. et al., 2011. Flood volcanism in the northern high latitudes of Mercury revealed by MESSENGER. Science 333, 1853–1856. http://dx.doi.org/10.1126/science.1211997.

Kasper, R.B., 1975. Cation and Oxygen Diffusion in Albite. Ph.D. Dissertation, Brown University, Providence, RI, 143pp.

Killen, R.M., Sarantos, M., Potter, A.E., Reiff, P., 2004. Source rates and ion recycling rates for Na and K in Mercury's atmosphere. Icarus 171, 1–19.

Lawrence, D.J. et al., 2011. Predictions of MESSENGER Neutron Spectrometer measurements for Mercury's north polar region. Planet. Space Sci. 59, 1665–1669. http://dx.doi.org/10.1016/j.pss.2011.07.001.

Lawrence, D.J. et al., 2013. Evidence for water ice near Mercury's north pole from MESSENGER Neutron Spectrometer measurements. Science 339, 292–296. http://dx.doi.org/10.1126/science.1229953.

Leblanc, F., Johnson, R.E., 2003. Mercury's sodium exosphere. Icarus 164, 261–281. http://dx.doi.org/10.1016/S0019-1035(03)00147-7.

Leblanc, F., Johnson, R.E., 2010. Mercury exosphere I. Global circulation model of its sodium component. Icarus 209, 280–300. http://dx.doi.org/10.1016/j.icarus.2010.04.020.

Leblanc, F. et al., 2007. Mercury's exosphere origins and relations to its magnetosphere and surface. Planet. Space Sci. 55, 1069–1092. http://dx.doi.org/10.1016/j.pss.2006.11.008.

Madey, T.E., Yakshinskiy, B.V., Ageev, V.N., Johnson, R.E., 1998. Desorption of alkali atoms and ions from oxide surfaces: Relevance to the origins of Na and K in atmospheres of Mercury and the Moon. J. Geophys. Res. 103, 5873–5887. http://dx.doi.org/10.1029/98JE00230.

McCubbin, F.M., Riner, R.A., Vander Kaaden, K.E., Burkemper, L.K., 2012. Is Mercury a volatile-depleted planet? Geophys. Res. Lett. 39, L09202. http://dx.doi.org/10.1029/2012GL051711.

Mura, A., Wurz, P., Lichtenegger, H.I.M., Schleicher, H., Lammer, H., Delcourt, D., Milillo, A., Orsini, S., Massetti, S., Khodachenko, M.L., 2009. The sodium exosphere of Mercury: Comparison between observations during Mercury's transit and model results. Icarus 200, 1–11. http://dx.doi.org/10.1016/j.icarus.2008.11.014.

Nittler, L.R. et al., 2011. The major element composition of Mercury's surface from MESSENGER X-ray Spectrometry. Science 333, 1847–1850. http://dx.doi.org/10.1126/science.1211567.

Paige, D.A. et al., 2013. Thermal stability of volatiles in the north polar region of Mercury. Science 339, 300–393. http://dx.doi.org/10.1126/science.1231106.

Peplowski, P.N. et al., 2011a. Mapping iron abundances on the surface of Mercury: Predicted spatial resolution of the MESSENGER Gamma-Ray Spectrometer. Planet. Space Sci. 59, 1654–1658. http://dx.doi.org/10.1016/j.pss.2011.06.001.

Peplowski, P.N. et al., 2011b. Radioactive elements on Mercury's surface from MESSENGER: Implications for the planet's formation and evolution. Science 333, 1850–1853. http://dx.doi.org/10.1126/science.1211576.

Peplowski, P.N. et al., 2012. Variations in the abundances of potassium and thorium on the surface of Mercury: Results from the MESSENGER Gamma-Ray Spectrometer. J. Geophys. Res. 117, E00L04. http://dx.doi.org/10.1029/2012JE004141.

Potter, A.E., Morgan, T.H., 1985. Discovery of sodium in the atmosphere of Mercury. Science 229, 651–653.

Potter, A.E., Morgan, T.H., 1986. Potassium in the atmosphere of Mercury. Icarus 67, 336–340.

Potter, A.E., Killen, R.M., Reardon, K.P., Bida, T.A., 2013. Observation of neutral sodium above Mercury during the transit of November 8, 2006. Icarus 226, 172–185. http://dx.doi.org/10.1016/j.icarus.2013.05.029.

Schleicher, H., Wiedemann, G., Wöhl, H., Berkefeld, T., Soltau, D., 2004. Detection of neutral sodium above Mercury during the transit on 2003 May 7. Astron. Astrophys. 425, 1119–1124.

Schlemm II, C.E. et al., 2007. The X-Ray Spectrometer on the MESSENGER spacecraft. Space Sci. Rev. 131, 393–415. http://dx.doi.org/10.1007/s11214-007-9248-5.

Shaw, H.R., 1972. Viscosities of magmatic silicate liquids; an empirical method of prediction. Am. J. Sci. 272, 870–893. http://dx.doi.org/10.2473/ajs.272.9.870.

Slater, V.P. et al., 2003. An evaluation of the igneous crystallization programs – MELTS, MAGPOX, and COMAGMAT, Part II: Importance of magmatic fO_2. Lunar Planet. Sci. 34. Abstract 1896.

Solomon, S.C., McNutt Jr., R.L., Gold, R.E., Domingue, D.L., 2007. MESSENGER mission overview. Space Sci. Rev. 131, 3–39. http://dx.doi.org/10.1007/s11214-007-9247-6.

Sprague, A.L., Kozlowski, R.W.H., Hunten, D.M., Schneider, N.M., Domingue, D.L., Wells, W.K., Schmitt, W., Fink, U., 1997. Distribution and abundance of sodium in Mercury's atmosphere, 1985–1988. Icarus 119, 506–527, doi:10.1006/icar.1997.5784.

Sprague, A.L., Schmitt, W.J., Hill, R.E., 1998. Mercury: Sodium atmospheric enhancements, radar-bright spots, and visible surface features. Icarus 136, 60–68, http://dx.doi.org/10.1006/icar.1998.6009.

Sprague, A. et al., 2007. Mercury's surface composition and character as measured by ground-based observations. Space Sci. Rev. 132, 399–431. http://dx.doi.org/10.1007/s11214-007-9221-3.

Stockstill-Cahill, K.R., McCoy, T.J., Nittler, L.R., Weider, S.Z., Hauck II, S.A., 2012. Magnesium-rich crustal compositions on Mercury: Implications for magmatism from petrologic modeling. J. Geophys. Res. 117, E00L15. http://dx.doi.org/10.1029/2012JE004140.

Taylor, G.J., Scott, E.R.D., 2003. Mercury. In: Davis, A.M. (Ed.), Meteorites, Comets, and Planets, Treatise on Geochemistry, vol. 1. Elsevier-Pergamon, Oxford, pp. 477–485.

Thompson, C.K. et al., 2003. An evaluation of the igneous crystallization programs – MELTS, MAGPOX, and COMAGMAT, Part I: Does one size fit all? Lunar Planet. Sci. 34. Abstract 1681.

Vasavada, A.R., Paige, D.A., Wood, S.E., 1999. Near-surface temperatures on Mercury and the Moon and the stability of polar ice deposits. Icarus 141, 179–193, http://dx.doi.org/10.1006/icar.1999.6175.

Vervack Jr., R.J. et al., 2012. Mercury's complex exosphere: Results from MESSENGER's third flyby. Science 329, 672–675. http://dx.doi.org/10.1126/science.1188572.

Weider, S.Z., Nittler, L.R., Starr, R.D., Byrne, P.K., Denevi, B.W., Solomon, S.C., 2012. Chemical heterogeneity on Mercury's surface revealed by the MESSENGER X-Ray Spectrometer. J. Geophys. Res. 117, E00L05. http://dx.doi.org/10.1029/2012JE004153.

Yan, N., Leblanc, F., Chassefiere, E., 2006. Potential relations between Caloris basin and Mercury's sodium exosphere. Icarus 181, 348–362. http://dx.doi.org/10.1016/j.icarus.2005.11.002.

Zolotov, M.Yu., Sprague, A.L., Hauck II, S.A., Nittler, L.R., Solomon, S.C., Weider, S.Z., 2013. The redox state, FeO content, and origin of sulfur-rich magmas on Mercury. J. Geophys. Res. Planets 118, 138–146. http://dx.doi.org/10.1029/2012JE004274.